Imaging of Multiple Targets in Dense Scattering Media

H. L. Graber[1], J. Chang[2], R. L. Barbour[1,2]

[1]Department of Physiology and Biophysics, [2]Department of Pathology,
SUNY Health Science Center at Brooklyn,
450 Clarkson Avenue, Brooklyn, NY 11203

Abstract

Formulas for the response of a detector on the surface of a highly scattering random medium to a change in physical properties within the medium were deduced from a transport–theory–based linear perturbation model. These expressions are called *weight functions*. Position–dependent intensities and fluxes were computed for the interior of a twenty mean free pathlength diameter, infinitely long, nonabsorbing, homogeneous cylindrical medium. Numerical values for the weight functions were calculated from these data. Surface detector readings were computed for the homogeneous reference medium and for six target media, each of which contained an array of twelve or thirteen thin, infinitely long rods embedded in the cylinder as a perturbation. The rods had a positive absorption cross section and a smaller scattering cross section than the reference, such that the mean free pathlength was constant throughout each medium. The directly computed detector readings perturbations were compared to those calculated from the linear perturbation model; as expected, the agreement was very good for the weakest cross section perturbations and became steadily poorer as the perturbations increased. Two iterative algebraic image reconstruction algorithms are described; both were used to compute images of the six target media. One algorithm tends to correctly identify the location of the rods lying closest to the surface, but places the deeper ones bunched too closely together near the cylinder axis. The other tends to place the superficial rods too close to the surface. In addition, while it appears to identify heterogeneities on the cylinder axis correctly after relatively few iterations, the estimated cross section perturbation along the axis gradually goes to zero as the number of iterations increases. Still in all, the performance of these algorithms is probably as good as can be achieved using a first–order Born reconstruction (*i.e.*, no update of forward problem).

Background and Introduction

Methods currently available for functional medical imaging (*e.g.*, PET, SPECT, functional MRI) exhibit significantly poorer spatial and temporal resolution than that attainable with anatomical imaging devices (*e.g.*, x–ray CT, ^{1}H–MRI). For techniques involving use of ionizing radiation, safety requirements place an upper limit on the employable doses. For those based on magnetic resonance, the net measured signal arises from the very slight difference between the population fractions of nuclei in different spin states; taken together with the very low absolute concentrations in biological tissues of all NMR–participating isotopes *other than* ^{1}H, the result is a very weak net source. As a consequence of these factors, functional imaging techniques typically require long signal acquisition times, and this is an important reason for their limited resolution. Quite apart from this sort of consideration, functional imaging devices are large, fixed installations with large energy requirements and are not suitable for use in acute–care settings.

Functional imaging based on analysis of visible (Vis) and near infrared (NIR) light that has propagated through tissue is a promising alternative. It has long been known that many endogenous chromophores have different absorption spectra corresponding to their various chemical or electronic states [1], and that knowledge of the concentration distributions of these states can be directly related to the physiological state of the tissue. A large number of exogenous probes, such as fluorophores, whose optical behaviors are dependent on some feature of their physical or chemical environments, has also been developed. (One well–known example is FURA–2, a $[Ca^{2+}]$–dependent fluorophore.) In addition, the optical properties of many biological tissues have now been measured and catalogued [2]. In most circumstances, the only way Vis/NIR light can damage tissue is through heating it, so dose restrictions are not nearly as stringent as those on higher energy radiations. Also, the different chemical or electronic states of the compounds being probed do not "cancel out" as the nuclei with opposite spins do in an NMR measurement. Consequently, acquisition of optical imaging data could be done in much less time, and at much more frequent

intervals, than is possible for the other techniques. It also is reasonable to suppose, due to advances in optical source and detector technology, that the device ultimately developed for acquiring the data will be small, portable, inexpensive, and require little energy and no great expertise to operate.

Elastic scattering is the dominant mode of interaction between most biological tissues and Vis/NIR radiation. Development of algorithms for recovering images from multiply scattered light is a difficult but central aspect of the Vis/NIR imaging project. It is generally accepted that, except in very special circumstances, the wave properties of light can be ignored for these wavelengths and media [3]. Then the distribution of light energy in a medium with any given set of physical properties and source condition can be found by solving the linear Boltzmann transport equation [4]. The physical properties of the medium that principally affect the propagation of the light through it are the macroscopic absorption and scattering cross sections (μ_a, μ_s), the differential scattering cross section, and the refractive index. These are expected to vary with position and/or direction in the medium; in this context, image reconstruction *means* computation of the values of one or more of these properties.

There is no known method for solving the general inverse problem of calculating the medium properties from a given set of measured intensities or fluxes. We have previously developed a perturbation model in which the inverse problem reduces to one of solving a system of linear equations,

$$\Delta \mathbf{R} = \mathbf{W}\Delta \mathbf{x}, \tag{1}$$

for a target medium that is discretized as a set of small, contiguous, non–overlapping voxels [5, and references therein]. This formulation is based on the assumption that we can specify a reference medium from which the target represents a small departure. It is a reasonable assumption, because the anatomical structure of the target and average "literature values" for the various tissue types within it will usually be known. In Equation (1), $\Delta \mathbf{x}$ is a vector whose elements are the differences in the individual voxels between the target and reference values of the physical properties under study, $\Delta \mathbf{R}$ is a vector whose elements are the differences between corresponding detector readings for the target and reference, and $\mathbf{W}$ is the appropriate *weight* matrix. That is, the model asserts that each detector reading perturbation is some linear combination of the interior perturbations. Accordingly, the ij^{th} element of $\mathbf{W}$ is $w_{ij} = \partial R_i / \partial x_j$, evaluated at the reference medium value of x_j.

A crucial test of an imaging algorithm is its ability to reconstruct media containing many regions in which the target and reference properties differ. The reconstruction inaccuracy is expected to increase as the distances between these regions decrease and/or $|\Delta x|$ in the voxels within them increases, for under these conditions the true relation between Δx and ΔR becomes increasingly nonlinear [6]. We have demonstrated successful image reconstructions of simply structured media [5,7–11], by which we mean the reference medium is homogeneous and the target differs from it in a finite number of regions with regular convex geometries. These reconstructions made use of algorithms that solve Equation (1) or a variant thereof (see Theory: Image Reconstruction; SART–type Algorithm). They have employed both computer–generated [5,7,8] and experimental [8–11] detector readings, but in all cases in which qualitatively very accurate images were obtained, the target medium contained only a small number (1–2) of heterogeneities. When there was a larger number (13) of more closely spaced heterogeneities, the quality of the reconstructed images was substantially poorer [7,8]. However, precisely in order to determine how large a perturbation algorithms based on solving Eq. (1) could handle, these were black–body absorbers ($\mu_a = \infty$). For the work reported on here, the black bodies were replaced by three different finite levels of μ_a and μ_s perturbations. Monte Carlo simulations were performed to calculate detector readings for both the reference and target media. Next, the deepest–lying heterogeneity was removed, and an additional set of detector readings was generated. Independent simulations were performed to compute the interior light intensity and flux distributions of the reference medium; these data were subsequently used for calculation of weight functions. Time–resolved detector readings and interior light intensity and flux distributions were computed, and subsequently integrated to obtain the corresponding time–independent (CW) quantities. Two algorithm variants were used to reconstruct images from each of the six sets of detector readings. The results of only the CW computations are presented and discussed in this report.

Theory

Perturbation Model; Weight Functions

In the following, we assume the physical properties that affect light propagation in the reference and target media are isotropic. That is, the absorption and scattering cross sections are functions of position only, and the differential scattering cross section is a

function of only position and of the angle between the directions of the incident and scattered photons. The appropriate CW linear transport equation for such a medium is

$$s(\mathbf{r},\Omega) + \int_{4\pi}\mu_s(\mathbf{r},\Omega'\cdot\Omega)\phi(\mathbf{r},\Omega')d\Omega' - \Omega\cdot\nabla\phi(\mathbf{r},\Omega) - \mu_T(\mathbf{r})\phi(\mathbf{r},\Omega) = 0,$$ (2)

where

Ω = direction unit vector

$d\Omega$ = differential solid angle about the direction Ω of photon motion,

$\phi(\mathbf{r},\Omega)$ = angular intensity at position $\mathbf{r}$ in direction Ω [photons / area / solid angle / time],

$s(\mathbf{r},\Omega)$ = angular source density at position $\mathbf{r}$ in direction Ω [photons / volume / solid angle / time],

$\mu_s(\mathbf{r},\Omega'\cdot\Omega)$ = macroscopic differential scattering cross section at position $\mathbf{r}$ from direction Ω' into direction Ω [1 / length / solid angle],

$\mu_s(\mathbf{r}) = \int_{4\pi}\mu_s(\mathbf{r},\Omega\cdot\Omega')d\Omega'$ = macroscopic scattering cross section at position $\mathbf{r}$ [1 / length], (by assumption, the result is independent of Ω).

$\mu_a(\mathbf{r})$ = macroscopic absorption cross section at position $\mathbf{r}$ [1 / length],

$\mu_T(\mathbf{r}) = \mu_a(\mathbf{r}) + \mu_s(\mathbf{r})$ = macroscopic total cross section at position $\mathbf{r}$ [1 / length].

The reciprocal of $\mu_T(\mathbf{r})$ is the position–dependent mean free pathlength (mfp). We express all cross sections in units of mfp^{-1}; area and volume in mfp^2 and mfp^3, respectively; time in mean free times (mft), where one mft is the time required for a photon to travel a distance of one mfp; and solid angles in steradians (sr). The effect of a perturbation was determined by replacing $\mu_T(\mathbf{r})$ with $\mu_T(\mathbf{r}) + \Delta\mu_T(\mathbf{r})$ and $\phi(\mathbf{r},\Omega)$ with $\phi(\mathbf{r},\Omega) + \Delta\phi(\mathbf{r},\Omega)$ in Equation (2), multiplying out and gathering sets of like terms, and then truncating terms proportional to $\Delta\mu_T(\mathbf{r})\Delta\phi(\mathbf{r},\Omega)$. The last step embodies our basic linearity assumption, which is valid for sufficiently small $\Delta\mu_T(\mathbf{r})$.

Let a detector that measures angular intensity be located at $(\mathbf{r}_d,\Omega_d)$. In the linear regime, the net detector response perturbation, ΔR, due to any number of localized μ_T perturbations is simply the sum of the effects of each one considered separately. Therefore, the difference between corresponding detector responses for the reference and target media is

$$\Delta R = \int_V w_T(\mathbf{r})\Delta\mu_T(\mathbf{r})d^3r = \int_V\left[w_a(\mathbf{r})\Delta\mu_a(\mathbf{r}) + w_s(\mathbf{r})\Delta\mu_s(\mathbf{r})\right]d^3r,$$ (3a)

where $w_a(\mathbf{r})$, $w_s(\mathbf{r})$, and $w_T(\mathbf{r})$ are the appropriate weight functions at $\mathbf{r}$. When the medium is discretized into voxels sufficiently small that it can be assumed the physical properties do not vary appreciably within a voxel, the form of Equation (3a) becomes instead

$$\Delta R_i = \sum_{j=1}^{J} w_{T,ij}\Delta\mu_{T,j} = \sum_{j=1}^{J}\left(w_{a,ij}\Delta\mu_{a,j} + w_{s,ij}\Delta\mu_{s,j}\right).$$ (3b)

Many detector readings combined give rise to a linear system, as indicated in Equation (1).

Phenomenologically, the ΔR produced by the $\Delta\mu_T$ in any given voxel is proportional to the number of photons from the source (per incident photon) that propagate through the voxel. It is also proportional to the number, per photon than leaves the voxel, that are detected by the selected detector. Under the assumptions stated above, the corresponding mathematical expression for ΔR is [12]

$$\Delta R = \int_V\int_{4\pi}\left[-\phi(\mathbf{r},\Omega)\Delta\mu_T(\mathbf{r}) + \int_{4\pi}\phi(\mathbf{r},\Omega')\Delta\mu_s(\mathbf{r},\Omega\cdot\Omega')d\Omega'\right]\phi^+(\mathbf{r},\Omega)d\Omega d^3r,$$ (4)

where $\phi^+(\mathbf{r},\Omega)$, the *adjoint* angular intensity, is the angular intensity at $(\mathbf{r}_d,\Omega_d)$ due to a unit–strength source at $(\mathbf{r},\Omega)$. Define:

$$\phi(\mathbf{r}) = \int_{4\pi} \phi(\mathbf{r},\Omega)d\Omega = \text{ intensity,}$$

$$\mathbf{J}^*(\mathbf{r}) = \int_{4\pi} \Omega \cdot \phi(\mathbf{r},\Omega)d\Omega = \text{ flux,}$$

$$\phi(\mathbf{r}) = \int_{4\pi} \phi^*(\mathbf{r},\Omega)d\Omega = \text{ adjoint intensity,}$$

$$\mathbf{J}^*(\mathbf{r}) = \int_{4\pi} \Omega \cdot \phi^*(\mathbf{r},\Omega)d\Omega = \text{ adjoint flux,}$$

$$g(\mathbf{r}) = \frac{\int_{4\pi} (\Omega \cdot \Omega')\mu_s(\mathbf{r},\Omega \cdot \Omega')d\Omega'}{\mu_s(\mathbf{r})} = \text{ anisotropy factor.}$$

Note that $g(\mathbf{r}) = \langle\cos\theta\rangle$, where θ is the angle between the initial and final directions of a scattered photon. Next, we expand the angular intensity and adjoint angular intensity in Equation (4) in spherical harmonics, Y_{ml}, and the differential scattering cross section in Eq. (4) in partial waves, P_l. Assuming the anisotropy of the angular intensities is sufficiently weak that the expansions may be truncated after $l = 1$, and that $g(\mathbf{r})$ is not affected by any perturbation in $\mu_s(\mathbf{r})$, we obtain the expressions for weight functions shown in Table 1 [12]. The *transport cross section*, $\mu_{tr}(\mathbf{r})$, that appears in the Table is defined as $\mu_{tr}(\mathbf{r}) = \mu_a(\mathbf{r}) + [1 - g(\mathbf{r})]\mu_s(\mathbf{r})$; its reciprocal is the *transport mfp*. In practice, by using μ_{tr}^{-1} rather than μ_T^{-1} as the distance unit, transport problems in media with moderate degrees of scattering anisotropy can be recast as isotropic scattering problems on distance scales $\geq \mu_{tr}^{-1}$. Note also that the appropriate expression for $w_a(\mathbf{r})$ depends on the choice of constraint; a complementary physical property must be assumed to be fixed.

Table 1: Weight Function Formulas

complementary physical property	weight for absorption	weight for complementary property
$\mu_s(\mathbf{r})$	$w_a(\mathbf{r})\big|_{\mu_s(\mathbf{r})} = \frac{1}{4\pi}\left[-\phi(\mathbf{r})\phi^*(\mathbf{r}) + 3\mathbf{J}(\mathbf{r})\cdot\mathbf{J}^*(\mathbf{r})\right]$	$w_s(\mathbf{r})\big|_{\mu_a(\mathbf{r})} = \frac{3[1 - g(\mathbf{r})]}{4\pi}\mathbf{J}(\mathbf{r})\cdot\mathbf{J}^*(\mathbf{r})$
$\mu_T(\mathbf{r})$	$w_a(\mathbf{r})\big|_{\mu_T(\mathbf{r})} = \frac{1}{4\pi}\left[-\phi(\mathbf{r})\phi^*(\mathbf{r}) + 3g(\mathbf{r})\mathbf{J}(\mathbf{r})\cdot\mathbf{J}^*(\mathbf{r})\right]$	$w_T(\mathbf{r})\big|_{\mu_a(\mathbf{r})} = \frac{3[1 - g(\mathbf{r})]}{4\pi}\mathbf{J}(\mathbf{r})\cdot\mathbf{J}^*(\mathbf{r})$
$\mu_{tr}(\mathbf{r})$	$w_a(\mathbf{r})\big|_{\mu_{tr}(\mathbf{r})} = \frac{-1}{4\pi}\phi(\mathbf{r})\phi^*(\mathbf{r})$	$w_{tr}(\mathbf{r})\big|_{\mu_a(\mathbf{r})} = \frac{3}{4\pi}\mathbf{J}(\mathbf{r})\cdot\mathbf{J}^*(\mathbf{r})$

Legend to Table 1 Expressions for weight functions according to Equation (3). Discretized versions, for use in Equation (1), are obtained by integrating $\phi(\mathbf{r})$, $\phi^*(\mathbf{r})$, $\mathbf{J}(\mathbf{r})$, and $\mathbf{J}^*(\mathbf{r})$ over the volume of each voxel. First column entry in each row is a physical property that may be perturbed independently of absorption; second column entry is the weight function for a absorption perturbation, subject to the constraint that the property specified in the first column is fixed; third column entry is the weight function for the complementary property, subject to the constraint that absorption is fixed. The third column entries in the first and second rows are necessarily identical, because $\Delta\mu_T(\mathbf{r}) = \Delta\mu_s(\mathbf{r})$ when $\mu_a(\mathbf{r})$ is fixed. All three entries in the third column are the same when $g(\mathbf{r}) = 0$ (*i.e.*, differential scattering cross section has a center of symmetry; isotropic scattering is a special case), because in that case $\mu_{tr}(\mathbf{r}) = \mu_T(\mathbf{r})$; likewise for the second and third row entries in the second column. These weight function expressions are specific for the case of CW illumination and detection.

Image Reconstruction; SART-type Algorithm

The SART (*i.e.*, *s*imultaneous *a*lgebraic *r*econstruction *t*echnique) was developed for imaging techniques involving forms of energy that pass through the target along straight ray paths [13]. It has been found to be useful as well for analyzing multiply scattered signals, but with much slower convergence [7]. The estimate of $\Delta\mathbf{x}$ is repeatedly updated according to the formula

$$\Delta x_j^{n+1} = \Delta x_j^n + \frac{\sum_{i=1}^{I} w_{ij} \dfrac{\Delta R_i - \sum_{j=1}^{J} w_{ij} \Delta x_j^n}{\sum_{j=1}^{J} w_{ij}}}{\sum_{i=1}^{I} w_{ij}}, \tag{5}$$

where I is the number of detector readings and J is the number of pixels/voxels in the image. $\Delta x_j^{n+1} = \Delta x_j^n$ when the second term on the right–hand side of Equation (5) is zero; while it is conceivable that this could happen due to cancellation of positive and negative terms in its numerator, it is very unlikely that a single set of Δx_j^n's could be found that would do so simultaneously for all $i = 1,2,...,I$. The only way the second term is likely to be zero for all i is if each term in its numerator equals zero separately, $i.e.$, $\Delta \mathbf{x}^n$ equals the true $\Delta \mathbf{x}$. The original developers of SART found, and empirical tests in our laboratory confirm, that it converges rapidly, often in a single iteration, when applied to straight–line tomography problems. Our (unpublished) studies showed that the convergence is most rapid for linear systems in which the matrix has a special structure likely to be found in this type of problem. This is a matrix in which all rows have the same sum (because all rays intersect about the same number of pixels) and all columns have the same sum (because all pixels are intersected by about the same number of rays). As the matrix structure deviates more and more from this idealized one, the rate of convergence falls, but the correct solution is eventually reached in most cases.

A different practical problem that arises in the type of image reconstruction problem we have undertaken is that absolute experimental quantification of ΔR is very difficult. This led us to attempt development of an image reconstruction algorithm based on *relative* detector readings changes, $(\Delta R/R_0)_i$, where R_0 denotes the reference medium detector response. The calibration requirements for accurate determination of $\Delta R/R_0$ are far less stringent than those needed to accurately measure the absolute values of either R_0 or ΔR. (An additional advantage to the use of the relative changes is that simple inspection can yield information useful for constraining the set of possible solutions that is not readily apparent from inspection of the absolute changes. For example, both R_0 and ΔR ordinarily are greatest for those detectors closest to the source and fall rapidly as the source/detector separation increases. However, $\Delta R/R_0$ is minimal for detectors near the source unless there is a heterogeneity lying close to the surface. That is, simple inspection provides information about the minimum depth at which a significant heterogeneity may lie.)

The first algorithm we developed, on purely heuristic grounds, iteratively updates the image according to the formula

$$\Delta y_j^{n+1} = \Delta y_j^n + \frac{\sum_{i=1}^{I} w_{ij} \left[\left(\dfrac{\Delta R}{R_0} \right)_i - \dfrac{\sum_{j=1}^{J} w_{ij} \Delta y_j^n}{\sum_{j=1}^{J} w_{ij}} \right]}{\sum_{i=1}^{I} w_{ij}}, \tag{6}$$

Here, the symbol for the unknown has been changed, to indicate that the quantity ("image intensity") being computed is not one of the physical cross sections, and its quantitative value is not easily interpretable. The formal similarity between this algorithm and SART was noted subsequently, and it was given the name "SART–type." Tests of this algorithm on both computed [5,7] and experimental [9–11] detector readings data for simply structured media give results whose qualitative structure is very accurate and contain few artifacts. Formally, by setting the bracketed expression in Equation (6) to zero, it can be shown that the linear system this algorithm is actually solving is

$$\mathbf{W}\Delta \mathbf{y} = \begin{bmatrix} \Delta R_1 \sum_{j=1}^{J} w_{1j} \Big/ R_{0,1} \\ \vdots \\ \Delta R_I \sum_{j=1}^{J} w_{Ij} \Big/ R_{0,I} \end{bmatrix}. \tag{7}$$

Therefore, the relation between Δy and Δx is

$$\Delta y = \mathbf{W}^{-1}\mathbf{Q}\mathbf{W}\Delta x, \qquad (8)$$

where $q_{ij} = \dfrac{\sum_{j=1}^{J} w_{ij}}{R_{0j}}\delta_{ij}$, and assuming $\mathbf{W}$ has a well–defined inverse. That is, each element of Δy is some linear combination of all the elements of Δx; note that if all q_{ii} are equal, then Δy is directly proportional to Δx.

Image Reconstruction; rSART Algorithm

Empirical studies show that in general all q_{ii} are *not* equal. There is a positive correlation between $\sum_{j=1}^{J} w_{ij}$ and R_{0j}, but for the model media used in the work presented here the ratio is on the order of one for detectors closest to sources and on the order of one hundred for those farthest from them. Therefore, the following modification of Equation (6) was proposed:

$$\Delta x_j^{n+1} = \Delta x_j^n + \frac{\sum_{i=1}^{I} w_{ij}\left[\left(\frac{\Delta R}{R_0}\right)_i^{(e)} - \left(\frac{\sum_{j=1}^{J} w_{ij}\Delta x_j^n}{R_{0j}}\right)^{(c)}\right]}{\sum_{i=1}^{I} w_{ij}}, \qquad (9a)$$

where the superscripts (e) and (c) indicate that the first parentheses contain an experimental quantity, the second a calculated one. This algorithm was given the name "rSART"; the initial letter serves to distinguish it from the original and to emphasize its use of relative detector readings changes. If Equation (9a) converges, the solution will be the true cross section perturbation, Δx. However, tests of Eq. (9a) showed that it typically diverges rapidly. It was found that this was the result of too large a correction being computed in each iteration, and the problem was easily remedied by modifying the iteration formula to

$$\Delta y_j^{n+1} = \Delta y_j^n + \frac{\sum_{i=1}^{I} w_{ij}\left[\left(\frac{\Delta R}{R_0}\right)_i^{(e)} - k\left(\frac{\sum_{j=1}^{J} w_{ij}\Delta y_j^n}{R_{0j}}\right)^{(c)}\right]}{\sum_{i=1}^{I} w_{ij}}, \qquad (9b)$$

for some $k < 1$. The solution to which this algorithm converges is $\Delta y = k\Delta x$. As of this writing, procedures for finding an optimal value of k are still under study; for the results reported here, the value used was simply $k = \left(\sum_{i=1}^{I}\sum_{j=1}^{J} w_{ij}\Big/I\right)^{-1}$.

Methods

Monte Carlo simulations were performed to compute the internal light distributions and the photon flux exiting 3–D cylindrical, isotropically scattering media. In all cases, the cylinder was infinitely long, its diameter was 20 mfp, and the light source was a monodirectional beam directed to a single point on the surface. The incident ray lay within a plane perpendicular to the axis; see Figure 1. Each incident photon underwent repeated scattering until it either escaped or was absorbed.
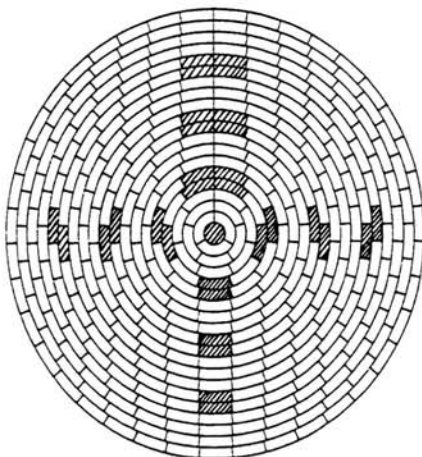
Figure 1

A

B
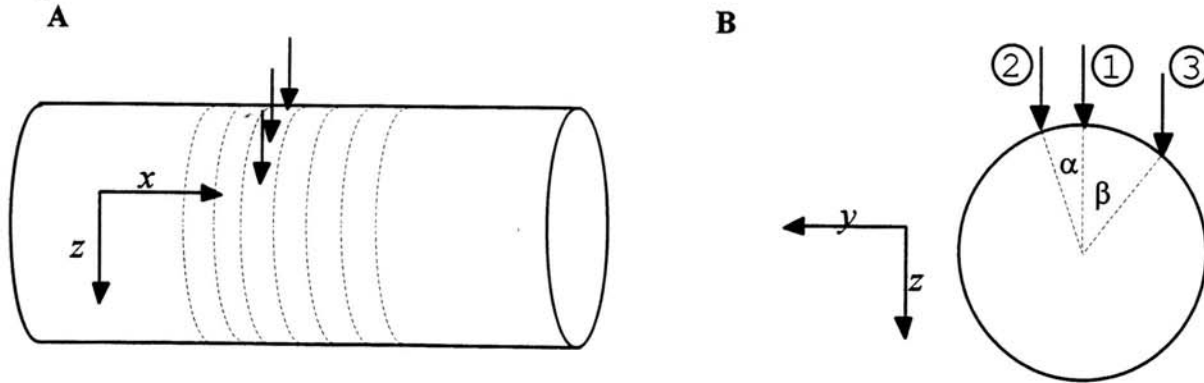
<u>Legend to Figure 1</u> Longitudinal (A) and transaxial (B) sketches of reference medium used for intensity and flux computations. Although the cylinder is infinitely long (*i.e.*, photons escape only through curve surface), collision events are scored in only ten layers of voxels to either side of the layer containing the source. At greater distances the intensity and flux are low enough to be safely neglected. The positive directions of the three Cartesian coordinate axes used for the flux computations are indicated. The angles α and β are approximately 22.02° and 38.68°, respectively. Non–normal source beam '2' lies exactly 3.75 mfp from the normal source beam, '1', in the y direction; non–normal source '3' lies exactly 6.25 mfp from '1' in the y direction. The cross sections are $\mu_a = 0$, $\mu_s = \mu_T = 1$ mfp^{-1}.

The internal intensity and flux distributions were computed for a homogeneous reference medium. The average collision density and it projections onto each of the three coordinate axes were computed in each of 8,400 voxels. These were arranged in 21 1–mfp–thick layers perpendicular to the cylinder axis; each voxel's volume was $\pi/4$ mfp^3 (*i.e.*, $\pi r^2 h/400$); see Figure 2. The output was reported in units of collisions/unit volume/incident photon; intensity is the ratio of the collision density to μ_T. The medium was nonabsorbing; each history was terminated when the photon escaped from the medium. There was no internal reflection at the boundary, as in the case of an object immersed in a transparent index–matching fluid. A total of 3×10^8 photons was launched into the medium from each of the three source locations indicated in Figure 1. The average number of collisions per history varied from ~26 for the normally directed source down to ~22 for the most grazing source.
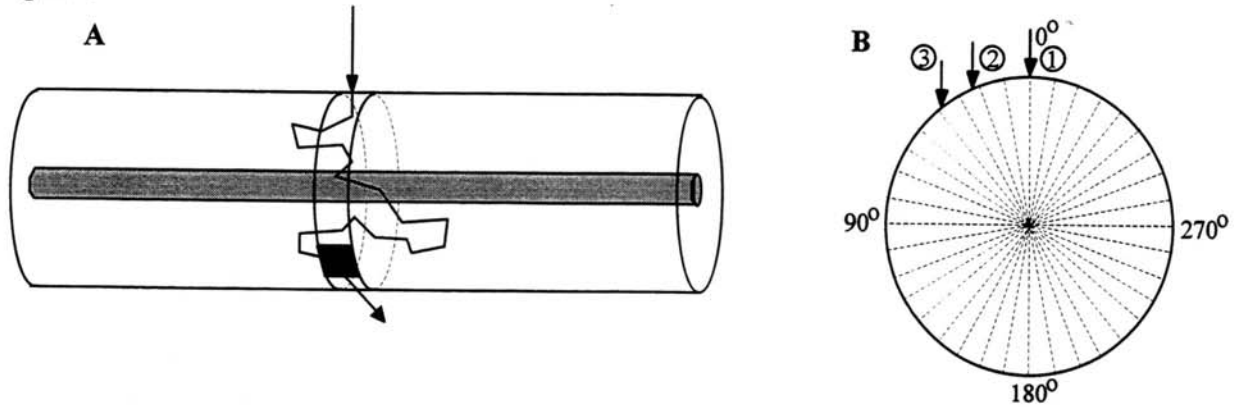
Figure 2

<u>Legend to Figure 2</u> Transaxial sketch of a cylinder, showing the pattern of voxels in which the intensity and flux were computed. While the voxel shape is different in each shell a constant distance from the axis, each voxel has the same volume. This pattern is convenient to work with because when a second copy is rotated through some angle and overlain on the original, as in calculating weight functions, each voxel in the one set overlaps with exactly one or two, and in the same shell, of the other. The shaded voxels in the sketch are those intercepted by one of the thirteen rods in the target media.

Detector readings were calculated in separate simulations from those that computed the collision densities; see Figure 3. The cylinder's surface was divided into twenty one bands by planes perpendicular to its axis, with the central band bisected by the plane containing the source. The readings of detectors in only the central band were actually used by the reconstruction algorithms. Each band was divided into thirty six congruent areas by lines parallel to the axis. Each of the resulting 756 patches

had an area of $5\pi/9$ mfp^2 (*i.e.*, $2\pi rh/36$), and a separate count was kept of photons exiting through each one. That is, the detectors modeled in these computations were cosine detectors at the surface, evenly spaced at 10° intervals about the cylinder.
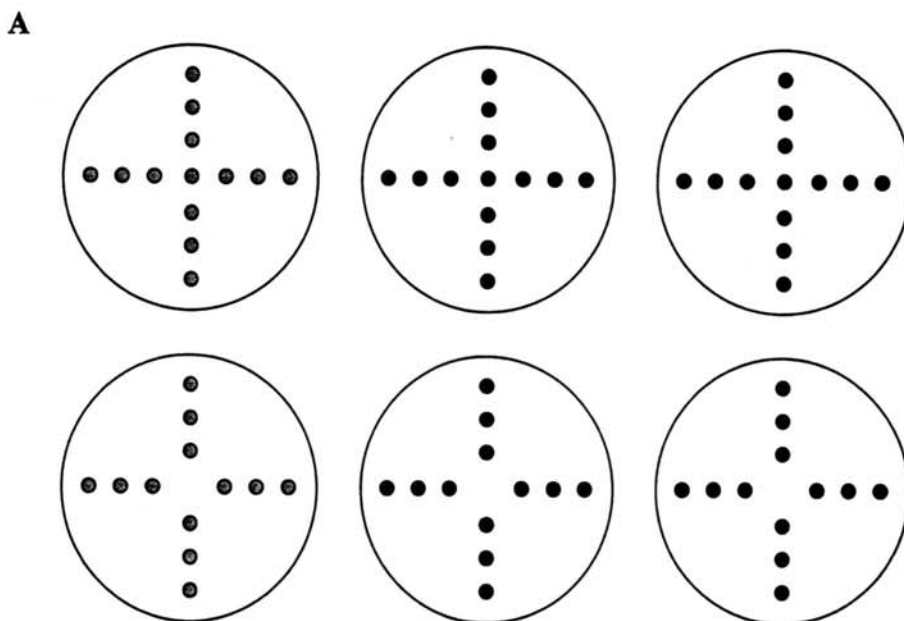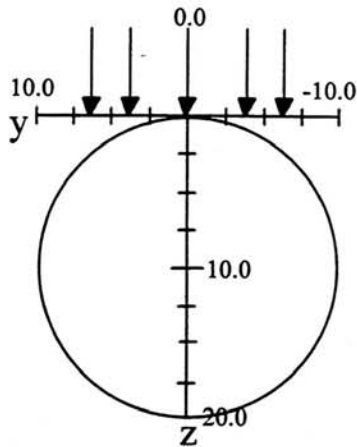
Figure 3

Legend to Figure 3 Longitudinal (A) and transaxial (B) sketches of cylinder, showing the partitioning of the surface into patches each of which is the site of a cosine detector. A) Dark shaded area is one such patch, located in the central band of detectors, *i.e.*, the one bisected by the plane containing the source beam and perpendicular to the cylinder axis. Also shown are one of the rods (light shading, not drawn to scale) used a heterogeneity in the target media, and a possible path for a photon entering and exiting at the indicated points. For the particular source/detector pair illustrated, this sort of path is much more likely than one that contains only a single scattering event, or one in which the photon remains within the central layer of voxels. B) Each band contains thirty six detectors, each subtending a 10° central angle.

Detector readings were computed for the homogeneous reference medium and for each of six distinct target media, whose structures are shown in Figure 4. The heterogeneity consisted of twelve or thirteen, infinitely long, .5–mfp–diameter rods in a fourfold symmetric cruciform array. Each rod was simultaneously more strongly absorbing and more weakly scattering than the reference medium. These were balanced in every case, *i.e.*, $\Delta\mu_s = -\Delta\mu_a$, so that μ_T was unperturbed. The three perturbation magnitudes modeled were $\Delta\mu_a = \mu_T$, $\Delta\mu_a = 0.10\mu_T$, and $\Delta\mu_a = 0.01\mu_T$. Detector readings were computed for each of the three source locations indicated in Figures 1 and 3.

Figure 4

B

A) Sketches of transaxial sections through the six target media modeled in the detector readings simulations. Three (top row) contained thirteen thin rods (.25 mfp radius, infinitely long), while the rod lying on the cylinder axis was absent from the other three (bottom row). Both μ_a and μ_s were perturbed, but μ_T was not. The three shadings denote the three perturbation magnitudes, $\Delta\mu_a = -\Delta\mu_s = 0.01\mu_T$ (left column), $\Delta\mu_a = -\Delta\mu_s = 0.10\mu_T$ (middle column), $\Delta\mu_a = -\Delta\mu_s = \mu_T$ (right column). B) Coordinates of rod axes are indicated by tic marks on the y and z axes. Also shown are the y coordinates of the source beams. Reconstruction algorithms took full advantage of the targets' symmetry, so the three detector readings computations amount to four views, with five source beam positions per view.

The number of photon histories simulated in the computations was 4×10^8 for the weakest of the perturbation magnitudes, 2×10^8 for the others. A correlated sampling technique was employed to reduce the statistical errors associated with these simulation results. Each photon in a target medium followed exactly the same trajectory as its counterpart in the reference medium. If it had a collision inside one of the rods, it was always absorbed in the case of $\Delta\mu_a = \mu_T$. In the cases of $\Delta\mu_a = 0.10\mu_T$, and $\Delta\mu_a = 0.01\mu_T$, a random variable uniformly distributed between zero and one was sampled, and on the basis of the sampled number the photon was absorbed with a 10% or 1% probability, respectively. Each photon that was not absorbed in the interior contributed equally to the response of a reference medium detector and the detector at the same location on the target medium. This minimizes the effect of randomness on the difference between the readings of the paired detectors.

The weight function computations made use of a well–known reciprocity theorem: the detector response at $(\mathbf{r}_d, \Omega_d)$ due to a unit–strength source at $(\mathbf{r}, \Omega)$ is equal to the intensity at $(\mathbf{r}, -\Omega)$ due to a source $r(\mathbf{r}_d, -\Omega_d)$, where $r(\mathbf{r}_d, -\Omega_d)$ is the detector response function [14]. Thus, the adjoint can be computed as the solution to a forward problem, just as the intensity is. In calculating weight functions for the present work, we used the intensity and flux distributions generated for source '1', rotated through the appropriate central angles (see Figure 3B), for the adjoint intensity and flux. This introduced a systematic error into the weight function calculation, because these were the appropriate adjoints for a single–point, monodirectional, normally directed detector, while finite–area cosine detectors were modeled in the detector readings computations. For the particular examples of image reconstructions in this report, we assumed *a priori* knowledge of the fact that $\Delta\mu_T = 0$, computed the weight functions $w_a\big|_{\mu_T}$ (see Table 1) and reconstructed images of only the absorption cross section perturbation.

Images were reconstructed of all six target media using both the SART–type and rSART algorithms. We assumed *a priori* knowledge of the fact that $\Delta\mu_a \geq 0$, and incorporated a positivity constraint into the algorithm implementations. They also took full advantage of all symmetry elements, both longitudinal and transaxial, in the targets. Thus, it was not necessary either to translate the source in the x direction or to use sources and detectors with different x coordinates. In addition, because the targets have symmetry about both the y and z axes, the three source locations effectively become twenty, in four views with five source locations per view, and thirty six detectors per source. Thus, there are 720 source/detector pairs altogether and 400 unknowns, so the linear system is overdetermined if the rank of **W** is at least 400.

Results

Examples of the computed detector readings are shown in Figure 5. Detector locations are specified in terms of the central angle between the detector and the point of incidence of the *normally directed* source. That is, a given value for the angle is to be thought of as an *absolute* location in the angular coordinate of a fixed polar coordinate system, not as a *relative* angle between source and detector. Note that the curves of ΔR and $\Delta R/R_0$ vs. angle are not completely featureless, but exhibit peaks and "shoulders" at detector locations closest to the arms of the rod array.

A direct test of the linear perturbation model was carried out by directly computing, for each source/detector pair i, the
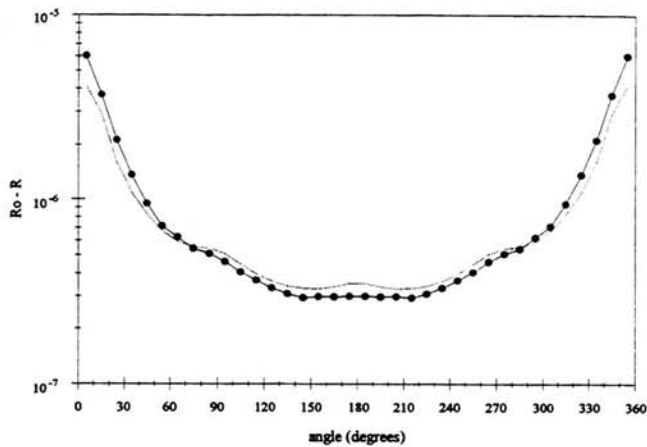
Figure 5

A

B

C
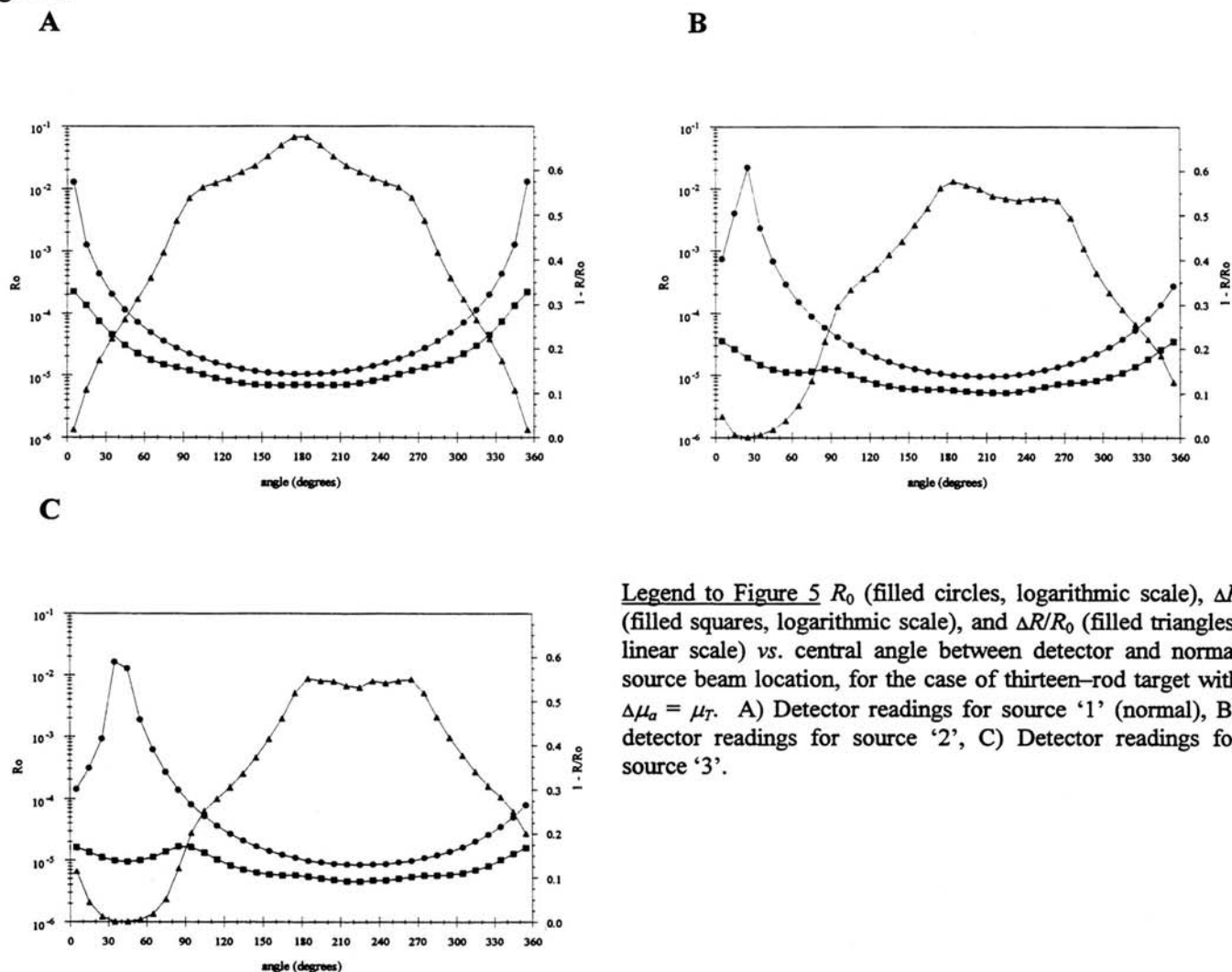
Legend to Figure 5 R_0 (filled circles, logarithmic scale), ΔR (filled squares, logarithmic scale), and $\Delta R/R_0$ (filled triangles, linear scale) vs. central angle between detector and normal source beam location, for the case of thirteen–rod target with $\Delta\mu_a = \mu_T$. A) Detector readings for source '1' (normal), B) detector readings for source '2', C) Detector readings for source '3'.

quantity $\sum_{j=1}^{J} f_j w_{a,ij} \Delta\mu_{a,j}$, where f_j = 0, 1/16, 1/8, or 1/4 is the fractional volume of voxel j that is occupied by a rod. As expected, the agreement between the ΔRs calculated from the model and those generated by the Monte Carlo simulations was closest for the case of the weakest perturbation. The model and simulation results are compared in Figure 6, for the case of the thirteen–rod target with $\Delta\mu_a = 0.01\mu_T$. The increasing departure of the simulation results from the predictions of the model with increasing perturbation magnitude is shown in Figure 7, where the ratios $\Delta R(\Delta\mu_a=0.10\mu_T)/\Delta R(\Delta\mu_a=0.01\mu_T)$ and $\Delta R(\Delta\mu_a=\mu_T)/\Delta R(\Delta\mu_a=0.10\mu_T)$ are plotted against detector angle for each of the three distinct sources. If the linear perturbation model were exactly correct, this ratio would be exactly 10.0 in both cases, for all sources and detectors. As can be seen in the figure, the average values of the ratios actually observed are ~8.5 and ~3.5, respectively, and there is some systematic variation with detector angle.

A hypothetical perfect reconstruction of a thirteen–rod target is shown in Figure 8. The twelve–rod ideal reconstruction would differ only in that the central peak would be absent. Although the rods all have circular geometric cross sections, the same absorption and scattering cross sections, and the same diameter, the image peaks corresponding to different rods have different heights and shapes. The height of the central peak is 0.25 because a rod occupies exactly one fourth of the volume of the central voxel in each layer. The difference in peak heights arises from the fact that only the rod on the cylinder axis lies entirely within a single voxel in each layer, while the others lie partially within two or four voxels; see Figure 2. Inspection of the same Figure likewise indicates the reason for the different peak shapes: the medium is discretized in a set of voxels that can accurately represent a perfect circle only if it is centered at the cylinder axis.
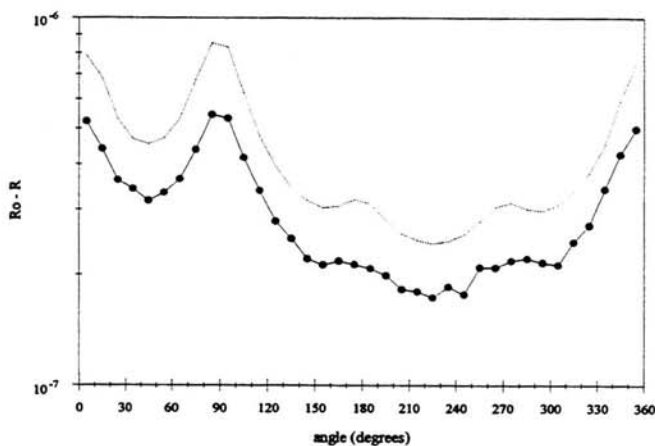
Figure 6

A

B
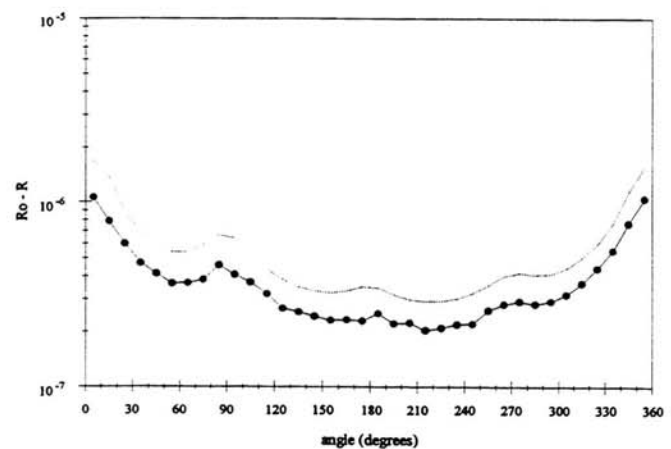
C

Legend to Figure 6 Comparison of detector reading computed by Monte Carlo simulations (filled circles, solid line) to those computed directly from the linear perturbation model (no symbols, dotted lines). Model values are computed by the formula $\Delta R_{c,i} = \sum_{j=1}^{J} f_j w_{a,ij} \Delta\mu_{a,j}$, where $f_j = 0$, 1/16, 1/8, or 1/4 is the fractional volume of voxel j that is occupied by a rod. Data are plotted for the thirteen-rod target with $\Delta\mu_a = 0.01\mu_T$. A) ΔR and ΔR_c, vs. detector angle, for source '1'; B) ΔR and ΔR_c, vs. detector angle, for source '2'; C) ΔR and ΔR_c, vs. detector angle, for source '3'.

Both the SART–type and rSART algorithms were used to reconstruct images based on the $\Delta R/R_0$ data from each of the six target media. The SART–type results for the thirteen–rod and twelve–rod targets with $\Delta\mu_a = \mu_T$ are shown in Figure 9. Each reconstruction was terminated after 2×10^4 iterations, in lieu of a convergence criterion. The corresponding results for the weaker perturbations are qualitatively similar and are not shown. A feature typically seen in images reconstructed by this algorithm is evident in these results: the most superficial peak on each "arm" of the array is very accurately located, while reconstructed locations of deeper structures are increasingly inaccurate and skewed in the direction of the cylinder axis (see Discussion). Because the five (four) deepest rods of the thirteen (twelve) are in reality quite closely packed, the result is that the corresponding image peaks coalesce into a single mass near the center. Another feature commonly seen in SART–type images also is apparent in these results: the nearly complete absence of artifacts in the regions between the arms of the array and at the surface. The difference between the thirteen–rod and twelve–rod images also is shown in the Figure. From this it is seen that although the twelve–rod image has positive image intensity at the center, where there ideally shouldn't be any, it is significantly lower there than in the thirteen–rod image. The distinctive biphasic appearance of the most superficial peaks in the image difference indicates that they are shifted to a slightly greater depth in the twelve–rod image relative to the thirteen–rod image.

The rSART results for the thirteen–rod and twelve–rod targets with $\Delta\mu_a = \mu_T$ are shown in Figure 10. In lieu of a convergence criterion, each reconstruction was terminated after 1.2×10^4 iterations. The corresponding results for the two weaker
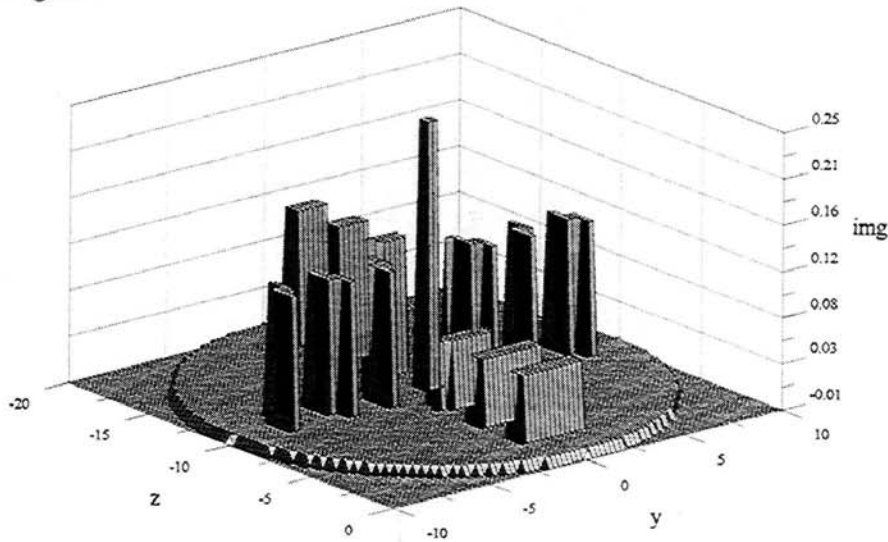
Figure 7

A

B

C
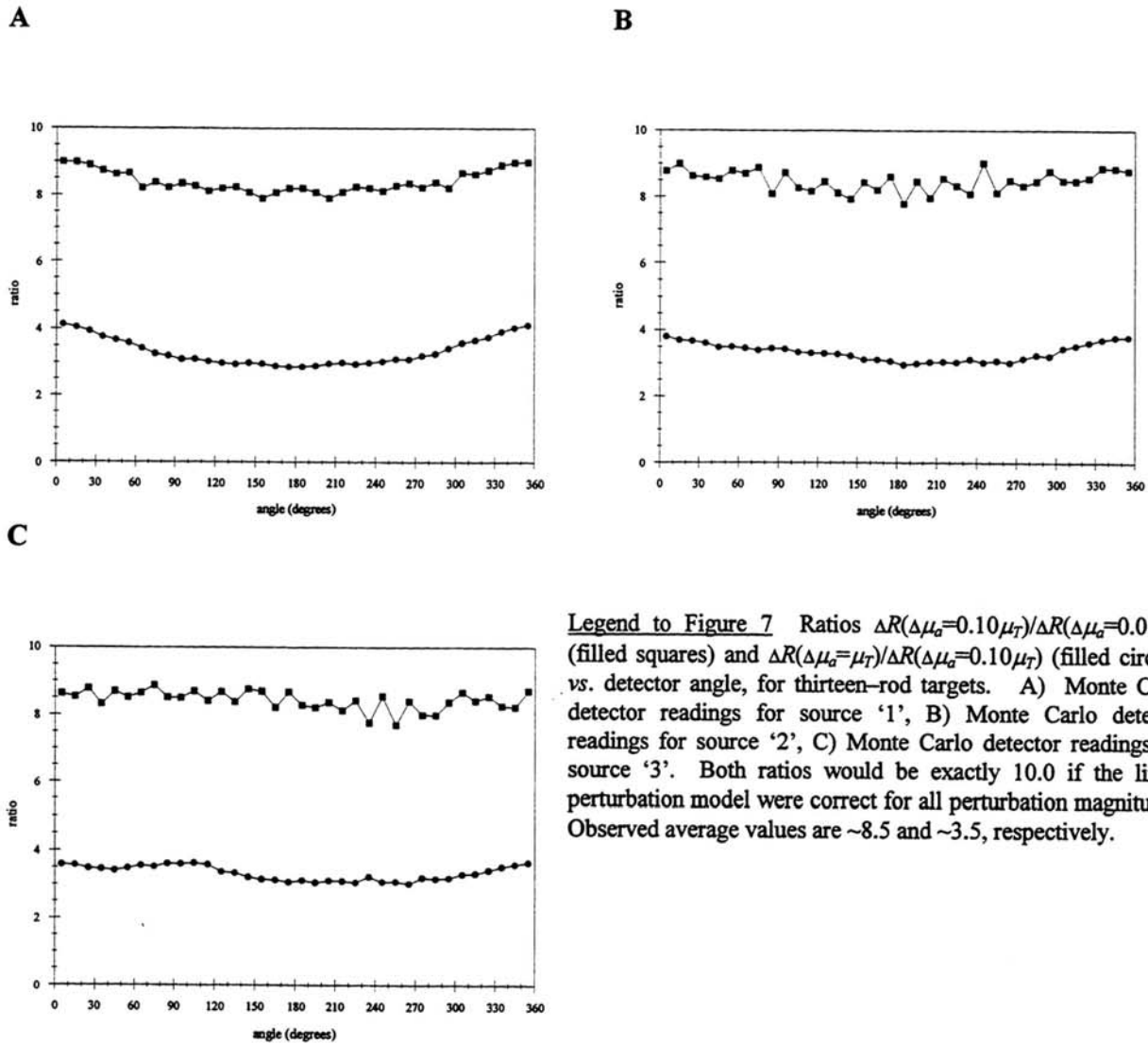
<u>Legend to Figure 7</u> Ratios $\Delta R(\Delta\mu_a=0.10\mu_T)/\Delta R(\Delta\mu_a=0.01\mu_T)$ (filled squares) and $\Delta R(\Delta\mu_a=\mu_T)/\Delta R(\Delta\mu_a=0.10\mu_T)$ (filled circles) *vs.* detector angle, for thirteen–rod targets.   A) Monte Carlo detector readings for source '1', B) Monte Carlo detector readings for source '2', C) Monte Carlo detector readings for source '3'. Both ratios would be exactly 10.0 if the linear perturbation model were correct for all perturbation magnitudes. Observed average values are ~8.5 and ~3.5, respectively.

perturbations are qualitatively similar and are not shown. This algorithm, as can be seen in these results, tends to produce images in which the depth of the most superficial rods and the perturbation magnitude at the center both are underestimated. This algorithm, like the SART–type, exhibits an encouraging tendency to suppress artifacts in the regions between arms of the array and near the surface. In addition, while the image values are underestimated in the vicinity of the cylinder axis, the rSART image difference shows, as in the case of the SART–type image difference, that the greatest difference between the thirteen–rod and twelve–rod images occurs, as it should, in that region.

Examination of the rSART images as a function of number of iterations (data not shown) revealed an interesting behavior. For the thirteen–rod, $\Delta\mu_a = \mu_T$ data, the image contained a peak on the cylinder axis that increased in magnitude for the first ~1,000 iterations, and slowly decreased to zero thereafter. The corresponding data for the $\Delta\mu_a = 0.10\mu_T$ and $\Delta\mu_a = 0.01\mu_T$ data gave also gave rise to a central peak, which reached its maximum value and then began to decrease after, respectively, ~3,000 and ~5,000 iterations. The corresponding twelve–rod data sets also gave rise to these transient peaks, but in every case it never reached the same maximum value as in the thirteen–rod case, and began to decrease after an appreciably smaller number of iterations.
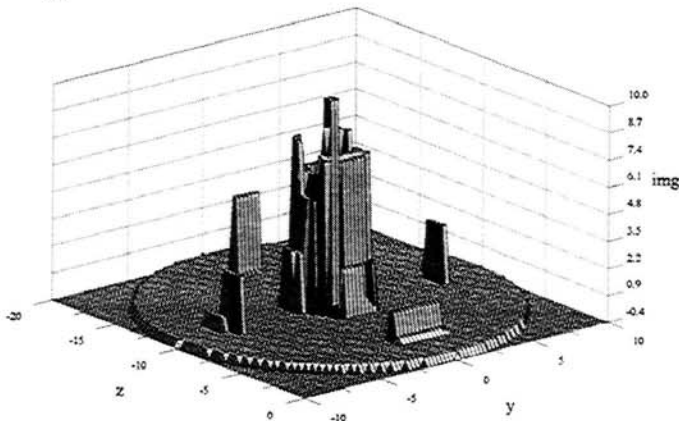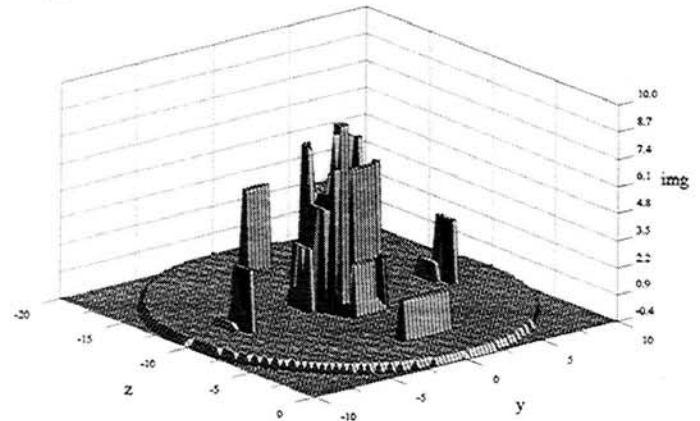
Figure 8

Legend to Figure 8 Ideal reconstruction of a thirteen–rod target medium. Although all rods have the same cross sections, the peak heights are different because some intercept four voxels in each layer, others only two, and the rod on the cylinder axis lies entirely within a single voxel.
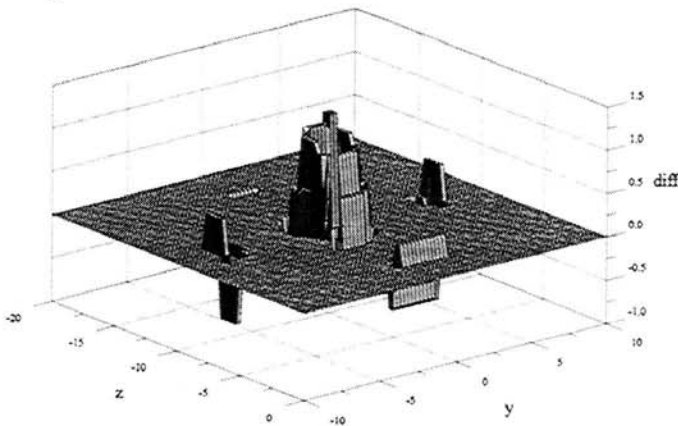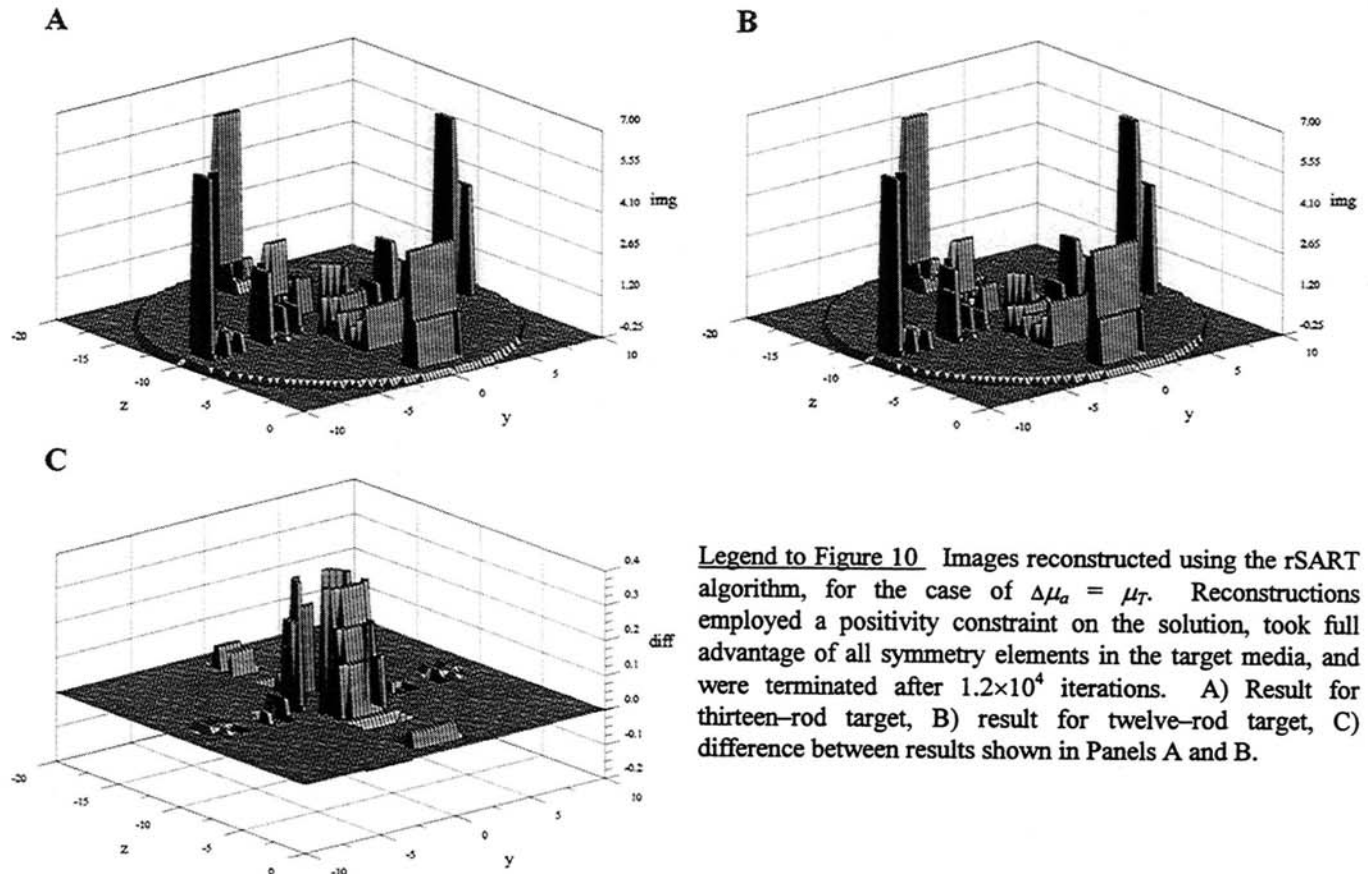
Figure 9

A

B

C

Legend to Figure 9 Images reconstructed using the SART–type algorithm, for the case of $\Delta\mu_a = \mu_T$. Reconstructions employed a positivity constraint on the solution, took full advantage of all symmetry elements in the target media, and were terminated after 2×10^4 iterations. A) Result for thirteen–rod target, B) result for twelve–rod target, C) difference between results shown in Panels A and B.

Figure 10

A

B

C

Legend to Figure 10 Images reconstructed using the rSART algorithm, for the case of $\Delta\mu_a = \mu_T$. Reconstructions employed a positivity constraint on the solution, took full advantage of all symmetry elements in the target media, and were terminated after 1.2×10^4 iterations. A) Result for thirteen–rod target, B) result for twelve–rod target, C) difference between results shown in Panels A and B.

Discussion and Conclusions

Both algorithms used to produce results presented in this report reconstructed images containing several features that lead us to conclude we have obtained positive results. This is so especially in light of the fact that we show here only images obtained on the basis of CW detector readings; we anticipate improved image quality when time–resolved and frequency–domain methods are employed. These features include the absence of any positive image values in the regions between the arms of the array of heterogeneous rods, resolution of the positive image intensity along each arm into several distinct regions, and the apparent suppression of artifacts in voxels near the surface. On the other hand, in detail, most regions containing positive image values are not in the correct location and the heights of the various peaks are not in the correct ratios.

The SART–type algorithm exhibits a tendency to reconstruct the most superficial rod locations correctly, but to coalesce the deeper rods into a single "multiplet" near the cylinder axis. The image value is maximum in the voxel lying on the cylinder axis, as it ought to be, in the thirteen–rod reconstructions; unfortunately, it is maximum in the same voxel, as it ought *not* to be, in the twelve–rod reconstructions. The difference between the thirteen– and twelve–rod images for the same perturbation magnitude indicates, however, that the algorithm does correctly sense that the two targets differ most in the immediate vicinity of the cylinder axis. Although we know the image intensity is positively correlated with the perturbation in μ_a, it is not clear just how it should be physically interpreted (see Methods: Image Reconstruction; SART–type Algorithm). This situation may be remedied if, as discussed below, future studies involving calculated ideal detector readings show just how the spatial distribution of physical cross section perturbations is "transformed" by this algorithm.

The rSART algorithm exhibits a tendency to reconstruct the most superficial rod locations too close to the surface and to underestimate the μ_a perturbations in deeper voxels. The image value in any voxel should be equal to the absolute $\Delta\mu_a$ there; in

the case of the images shown in Figure 10, it is necessary to correct for the specific value of the parameter k that was used to prevent divergence, and for the fact that the observed $\Delta R(\Delta\mu_a = \mu_T)/\Delta R(\Delta\mu_a = 0.01\mu_T)$ is ~29.75 instead of 100. When these corrections are made, the reconstructed $\Delta\mu_a$ in the most superficial peaks is ~0.136, very close to the theoretically expected value of 0.125. As the distance of these peaks from the surface is underestimated in the reconstructions and there is a general tendency for weight to decrease with increasing depth, the contributions of the most superficial rods to the total ΔR would be overestimated for most source/detector pairs. It is reasonable to suppose that the rSART algorithm compensated for this by underestimating $\Delta\mu_a$ in deeper–lying voxels.

A possible explanation that comes readily to mind for the errors in detail in the reconstructed images is that a linear perturbation model is inadequate for modeling the effect on detector responses of perturbations as extensive as those in the target media considered here. According to this argument, use of weight functions calculated for the reference medium is analogous to a first–order Born approximation; production of highly accurate reconstructed images ultimately entails resorting to an iterative process in which each successive image is taken as a new reference medium estimate, a corresponding set of weight functions is calculated for the new reference, and the image reconstruction problem is repeated. This is a very reasonable suggestion, and certainly not one to be dismissed out of hand. However, we conclude that other sources of error are more important in explaining the errors in the images reconstructed from the sets of detector readings perturbations for our six target media. The comparison of the detector readings generated by Monte Carlo simulations to those computed directly from the model for the weakest perturbation suggests that the model should be entirely adequate in this case. While inspection of Figure 6 does show that for almost all source/detector pairs the ΔR computed by the simulation is less than that computed from the model, consistent with the known tendency of shadowing of a heterogeneity by itself and by others in its vicinity to reduce ΔR below the expected value [6], the nearly parallel behavior of each ΔR curve and the corresponding model curve is striking. Examination of the ΔR ratios for different perturbation magnitudes shows that even though they are smaller than predicted by the model, they have very little dependence on the location of either source or detector. This would suggest that a qualitatively accurate reconstruction should be obtained even for the strongest perturbation, with the perturbation magnitude underestimated by about the same factor in each voxel. However, it is apparent that the reconstruction results are more than just quantitatively inaccurate (Figures 8–10). In light of the foregoing observations, this should not be *primarily* due to departures of the true relation between $\Delta \mathbf{R}$ and $\Delta \mathbf{x}$ from linearity.

Other issues that are always of great importance when using a numerical image reconstruction algorithm is the effects of systematic and random errors in the data on the result, and the effect of such factors as limited numerical precision in the computational platform used. These effects are frequently amplified as the number of iterations increases. Among the lines to be pursued in future work will be substitution of "ideal" detector readings computed directly from the linear model for those generated by simulations or experiment; these "data" will subsequently be corrupted by increasing degrees of systematic and/or random error. It is hoped that an outcome of these studies may be the development of corrections to apply to results of reconstructions such as those presented above. Other intended subjects for future studies are development of reconstruction methods employing time–resolved and time–harmonic data, and simultaneous reconstruction of μ_a and μ_s (or μ_T) perturbations.

Acknowledgments

References

1. O. W. van Assendelft, *Spectrophotometry of Haemoglobin Derivatives*, Charles C. Thomas, Springfield, IL, 1970.
2. F. A. Duck, *Physical Properties of Tissue*, chap. 3, Academic Press, San Diego, CA, 1990.
3. A. Yodh, B. Chance, "Spectroscopy and imaging with diffusing light," *Physics Today*, vol. 48, no. 3, pp. 34–40, 1995.
4. K. M. Case, P. F. Zweifel, *Linear Transport Theory*, Addison–Wesley, Reading, MA, 1967.
5. R. L. Barbour, H. L. Graber, Y. Wang, J. Chang, R. Aronson, "A perturbation approach for optical diffusion tomography using continuous–wave and time–resolved data," *Medical Optical Tomography: Functional Imaging and Monitoring*, G. Müller *et al.*, eds., SPIE vol. IS11, pp. 87–120, 1993.

6. H. L. Graber, R. L. Barbour, J. Chang, R. Aronson, "Identification of the functional form of nonlinear effects of localized finite absorption in a diffusing medium," *Proc. Optical Tomography, Photon Migration, and Spectroscopy of Tissue and Model Media: Theory, Human Studies, and Instrumentation*, SPIE vol. 2389, pp. 669–681, 1995.

7. J. Chang, R. Aronson, H. L. Graber, R. L. Barbour, "Imaging diffusive media using time–dependent and time–harmonic sources: dependence of image quality on imaging algorithms, target volume, weight matrix, and view angles," *Proc. Optical Tomography, Photon Migration, and Spectroscopy of Tissue and Model Media: Theory, Human Studies, and Instrumentation*, SPIE vol. 2389, pp. 448–464, 1995.

8. H. L. Graber, R. L. Barbour, J. Chang, "Algebraic reconstruction of images of a diffusive medium containing strong absorbers: comparative study of different illumination schemes and the effect of restricted view angle," *Proc. Optical Tomography, Photon Migration, and Spectroscopy of Tissue and Model Media: Theory, Human Studies, and Instrumentation*, SPIE vol. 2389, pp. 431–447, 1995.

9. H. L. Graber, J. Chang, J. Lubowsky, R. Aronson, R. L. Barbour, "Near infrared absorption imaging of dense scattering media by steady–state diffusion tomography," *Proc. Photon Migration and Imaging in Random Media and Tissues*, SPIE vol. 1888, pp. 372–386, 1993.

10. H. L. Graber, J. Chang, R. Aronson, R. L. Barbour, "A perturbation model for imaging in dense scattering media: Derivation and evaluation of imaging operators," *Medical Optical Tomography: Functional Imaging and Monitoring*, G. Müller *et al.*, eds., SPIE vol. IS11, pp. 121–143, 1993.

11. B. B. Das, J. Dolne, R. L. Barbour, H. L. Graber, J. Chang, M. Zevallos, F. Liu, R. R. Alfano, "Analysis of time–resolved data for tomographical image reconstruction of opaque phantoms and finite absorbers in diffusive media," *Proc. Optical Tomography, Photon Migration, and Spectroscopy of Tissue and Model Media: Theory, Human Studies, and Instrumentation*, SPIE vol. 2389, pp. 16–28, 1995.

12. R. Aronson *et al.*, manuscript in preparation.

13. A. H. Anderson, A. C. Kak, "Simultaneous algebraic reconstruction technique (SART): a superior implementation of the ART algorithm," *Ultrasonic Imaging*, vol. 6, pp. 81–94, 1984.

14. H. C. van de Hulst, *Multiple Light Scattering: Tables, Formulas, and Applications*, vol. 1, chap. 3, Academic Press, New York, NY, 1980.